Discovery of interpretable T_c descriptors in conventional superconductors guided by symbolic regression

Fang Han Lim [1,*] Jinbo Pan [1,2,†] and Shixuan Du [1,2,‡]

[1]*Beijing National Laboratory for Condensed Matter Physics, Institute of Physics, Chinese Academy of Sciences, Beijing 100190, China*
[2]*School of Physics, University of Chinese Academy of Sciences, Beijing 100049, China*

(Received 26 November 2025; accepted 13 April 2026; published 22 May 2026)

Advancement of superconductivity is hindered by complexity of underlying mechanisms. Machine learning models have potential to accelerate materials discovery but face data limitations and interpretability challenges. This study identifies material genes governing conventional superconductivity through systematic two-stage analysis, where atomic descriptors are directly related to their phonon-mediated mechanism, unlike unconventional superconductors where strong electronic correlations that go beyond the Bardeen-Cooper-Schrieffer paradigm dominate in the formation of pairing glue. We first apply the random forest classifier and regressor to 16 320 superconductors from NIMS database, screening over 114 MAGPIE and MEREDIG atomic descriptors to identify the 30 most important features. Combining these atomic descriptors with DFT-calculated bulk properties, we then perform SISSO (sure independence screening and sparsifying operator) symbolic regression on 60 carefully selected conventional superconductors. The resulting three-dimensional model [$R^2 = 0.778$, AFD (average factor difference) $= 1.173$] reveals optimal T_c requires an average of half filled or near half filled d electrons with moderate unfilled orbital heterogeneity. The discovered descriptors integrate d-valence electrons, unfilled orbitals, and electronegativity variations, providing actionable guidelines for materials design.

DOI: 10.1103/4pxk-z8ww

I. INTRODUCTION

Superconductivity, characterized by zero electrical resistance and magnetic field expulsion below critical temperature (T_c), has captivated scientists since its discovery by Onnes in 1911 [1]. The main reason for the sustained interest is the challenge of finding whether a room-temperature superconductor at ambient pressure is possible and, if yes, the mechanism(s) that enable it and the materials that exhibit it. These superconductors can be broadly categorized into two groups: conventional and unconventional. To date, the only widely acknowledged mechanism for realizing the superconducting state in a conventional superconductor is the Bardeen, Cooper, and Schrieffer (BCS) theory [2], according to which the formation of bound electron pairs, known as Cooper pairs in an s-wave, low-T_c conventional superconductor found in most elemental metals and simple alloys [3] is due to the electron-phonon interaction effectively overcoming the electron-electron repulsion at low energies. While BCS theory successfully explains conventional superconductors through electron-phonon interaction, unconventional superconductors such as cuprates [4], iron-based [5,6] compounds, and heavy fermion [7] systems continue to challenge our understanding with their intricate pairing mechanisms. Despite decades of intense theoretical, experimental, and computational effort, a microscopic theory of high-temperature superconductivity is not yet established [8], with each theoretical framework and experimental probe offering insights yet incomplete.

The quest for room-temperature superconductors has intensified the need for a deeper understanding of the fundamental material properties that govern superconducting behavior. While traditional approaches to discovering new superconductors have led to significant discoveries, they are inherently limited by the vast chemical space of possible materials and the complex interplay of multiple physical parameters that influence superconducting properties. In recent years, the emergence of materials informatics and artificial intelligence approaches has opened new avenues for understanding and predicting superconducting properties. The advent of artificial intelligence (AI) techniques using high-dimensional data representation in materials informatics has accelerated inverse design through property prediction, detecting hidden patterns in data sets and revealing complex relationships between material properties and structural representations [9–11]. Significant efforts have been devoted to applying AI approaches in superconductor research, particularly for the design of novel superconductors and prediction of their properties, especially T_c. Notable contributions include Choudhary *et al.* developing deep learning (DL) frameworks combining BCS-inspired screening with density functional theory and DL for designing high-T_c superconductors [12]. Le *et al.* applied variational Bayesian neural networks to predict T_c, demonstrating improved uncertainty quantification in superconductor property prediction [13]. Zhang *et al.* enhanced machine learning (ML) models by developing structural descriptors for robust prediction of T_c, incorporating both compositional and structural features [14,15]. Recent work has addressed data scarcity through generative approaches:

*Contact author: edwardlfh@iphy.ac.cn
†Contact author: jbpan@iphy.ac.cn
‡Contact author: sxdu@iphy.ac.cn

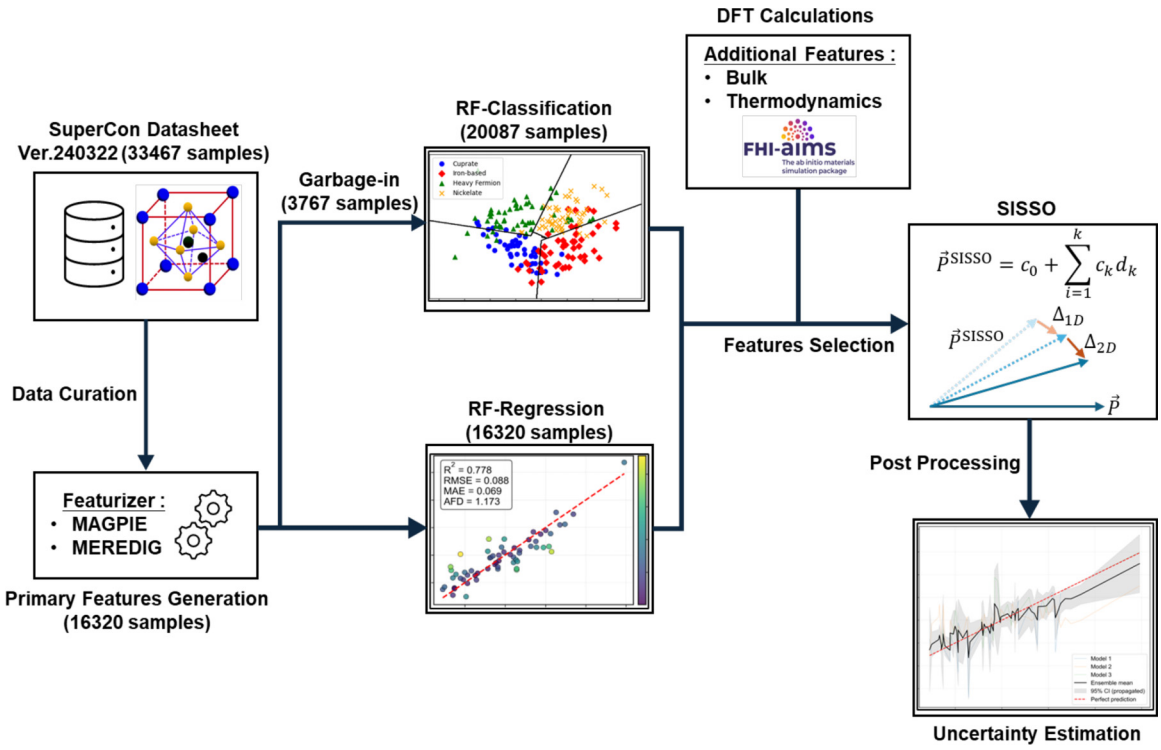

FIG. 1. Workflow of RF-SISSO model. Discovery of interpretable material descriptors through two main stages: (i) feature selections with random forest (RF) models and (ii) SISSO model which constructs optimal multidimensional expressions using symbolic regression and compressed sensing.

Chen *et al.* developed generative models for inverse design of inorganic solid materials [16] and cardiGAN approaches have been applied for design and discovery of multiprincipal element alloys [17].

However, many machine learning models operate as "black boxes," providing accurate predictions without offering interpretable insights into the underlying physics. This limitation has motivated the development of interpretable machine learning methods that can extract physically meaningful relationships from complex data sets. The sure independence screening and sparsifying operator (SISSO) method, developed by Ouyang *et al.* [18–20], represents a significant advancement in this direction. SISSO is a compressed-sensing-based approach that works to identify the most relevant descriptors or features, known as "material genes," that govern a particular property of interest in materials science. Unlike traditional machine learning algorithms that often produce complex, noninterpretable models, SISSO generates simple, analytical functionals that capture the essential physics underlying the target property [21–23].

However, SISSO's effectiveness is critically dependent on the quality and relevance of input features. With materials databases containing hundreds of potential descriptors, systematic feature selection becomes essential to identify the most physically meaningful properties. Random forest [24] methods (RF) have emerged as powerful tools for feature importance ranking, capable of handling high-dimensional data while providing robust importance measures that account for feature interactions.

In this study, we demonstrate a two-stage approach combining RF feature selection on large data sets with SISSO on carefully curated subsets to identify interpretable material genes controlling superconducting critical temperature, as illustrated in Fig. 1. Our methodology first employs RF to screen 114 atomic descriptors, identifying the 30 most important features (achieving $R^2 = 0.983$ for T_c prediction). These features, combined with 17 DFT-calculated properties, are then analyzed via SISSO to generate a three-dimensional analytical model ($R^2 = 0.778$; AFD $= 1.173$) that captures the essential physics of conventional superconductivity. To validate the interpretability-accuracy trade-off of our approach, we systematically compare SISSO's performance against other black-box methods. Then we conduct feature sensitivity analysis to extract physical relevance and analyze how SISSO-identified features connect to established theoretical frameworks in superconductivity. Ultimately, we aim to illuminate how T_c depends on and relates to a set of material descriptors within a known materials space. The resulting model reveals that optimal T_c emerges from synergistic interplay of electronic heterogeneity [$\sigma(Z_{\text{unf}}) > 2.0$], half-filled d-electron configurations ($n_d \approx 4$–5), sufficient unfilled orbitals ($\langle Z_{\text{unf}} \rangle > 6$), and intermediate electronegativity ($\langle \chi \rangle \approx 1.8$–2.0). Sensitivity analysis (SHAP, LIME, Sobol) validates these relationships and demonstrates that superconductivity requires collective optimization rather than maximization of individual parameters. Rather than merely cataloguing or predicting new material properties in isolation, we focus on uncovering sensitivities, dependencies, and structure-property relationships that govern T_c. While the approach can be extended to explore materials not yet synthesized, the core objective remains to characterize how target properties emerge from underlying material features.

II. METHODS

A. Creating data set

Superconductivity data used in the present work is extracted from MDR SuperCon Datasheet Ver. 240322 [25], a numerical data sheet for superconducting materials, which is made public by the National Institute for Materials Science (NIMS), containing approximately 33 465 materials entries. Comprehensive details on data handling in data set creation are listed in the Supplemental Material [26]. After rigorous data cleansing, 16 320 superconductors remained and were used in regression task. Also, a garbage-in approach was adopted to supplement the data set with 3767 samples, including both nonsuperconductors and material with no T_c reported to provide negative examples for classification tasks. While this curation process eliminated the most egregious data quality issues, some residual inconsistencies likely remain in the processed data set. However, the influence of such remaining anomalies on the overall statistical analysis is expected to be negligible.

For the SISSO analysis, a representative subset of 60 conventional superconductors was carefully selected to ensure balanced representation across all major structural and compositional categories. The selection encompassed elemental superconductors, binary and ternary alloys [3], A15-phase compounds [36], doped semiconductors [37], intercalated graphite systems [38], layered TMD [39], Chevrel phases [40], magnetic [41], and magnesium diboride [42] superconductors. The sampling approach was designed to capture the full diversity of conventional superconducting mechanisms while maintaining a data set of sufficient size for reliable statistical analysis yet manageable for comprehensive feature engineering and model interpretation.

B. Random forest method with Bayesian optimization cross validation

Random forest (RF) was selected due to its versatility and suitability for this investigation. This method offers several key advantages for superconducting materials prediction. For example, the RF method can capture complex nonlinear relationships without requiring assumptions about the functional form of predictor-target dependencies, unlike parametric methods such as linear regression. Additionally, the algorithm demonstrates robust performance with heterogeneous data sets, handling both numerical and categorical features without extensive preprocessing requirements such as scaling or normalization. The method also maintains stability in the presence of correlated predictors, which commonly affect other machine learning approaches. This strategy addresses the computational challenge of exploring high-dimensional feature spaces while maintaining model interpretability. Direct application of SISSO to all available descriptors is computationally prohibitive due to exponential scaling with a feature number; thus RF prescreening identifies the most informative subset for subsequent SISSO analysis. The initial feature space comprised over 200 descriptors generated using MAGPIE (Materials Agnostic Platform for Informatics and Exploration) [43] and MEREDIG [44] frameworks. 114 features were left after removing duplicate and zero entries. These included atomic properties, electronic characteristics, thermodynamic parameters, and statistical measures (mean, range, average deviation, etc.) computed across constituent elements; detailed calculations of these descriptors are described in the Supplemental Material [26].

We implemented both RF classification (RFC) and RF regression (RFR) to capture different aspects of the structure-property relationships. Following the Kohn-Luttinger theorem [45], which predicts superconducting instabilities at arbitrarily low temperature for any metallic system with repulsive interactions, materials with no observed superconductivity down to some finite temperature cannot be strictly labeled nonsuperconductors. We adopted a threshold-based classification ($T_c > 0.3$ K) rather than binary superconductor/nonsuperconductor labels. This choice corresponds to the practical limit of He 3 refrigeration, providing a more physically rigorous distinction between experimentally accessible superconductors and those requiring advanced dilution refrigeration techniques. Threshold sensitivity analysis confirms that the identified descriptors are robust to this threshold choice (Supplemental Material [26]). The RFC distinguished materials above/below this threshold, while the RFR predicted continuous T_c values.

C. SISSO methodology

The SISSO method [18,19] was implemented to identify the most relevant material descriptors governing T_c using preselected features from RF analysis, combining with properties calculated using FHI aims [46] and FHI vibes [47]. Full details of the DFT computational setup, including structural relaxation protocols, polymorph treatment, and phonon calculation parameters, are provided in the Supplemental Material [26]. DFT-calculated properties are important because they encode collective solid-state behavior that cannot be reconstructed from elemental descriptors through SISSO's operator set and attempting to do so would require SISSO to rediscover many-body quantum mechanics from atomic-level inputs, which is computationally infeasible given the doubly exponential scaling of the descriptor search space.

SISSO operates through a two-step process: sure independence screening (SIS) for feature selection and the sparsifying operator (SO) for descriptor construction. The algorithm begins with a set of primary features $(\psi_1, \psi_2, \ldots, \psi_n, \ldots, \Psi)$ and a set of unary and binary mathematical operators $\hat{h}_1, \hat{h}_2, \ldots, \hat{h}_n, \ldots, \hat{\mathcal{H}}$ to exhaustively construct rungs of candidate analytical expressions through recursive application. The SIS step ranks these candidates by Pearson correlation with the target property P, selecting the n_SIS most correlated features for S_1 to create one-dimensional models (descriptors). For higher dimensions, features most correlated with residuals from the best one-dimensional descriptors are selected for S_2, continuing iteratively. The SO then performs l_0-regularized optimization over feature subspaces ($S_1 \cup S_2$ for two-dimensional models) to identify the sparsest linear combination describing the target property:

$$\text{argmin}_{\mathbf{c}} \|\mathbf{P} - \mathbf{cd}\|^2 + \lambda \|c\|_0. \quad (1)$$

Here $\mathbf{d}$ and $\mathbf{c}$ represents the potential descriptors and coefficient, respectively, and $\|c\|_0$ denotes the number of nonzero

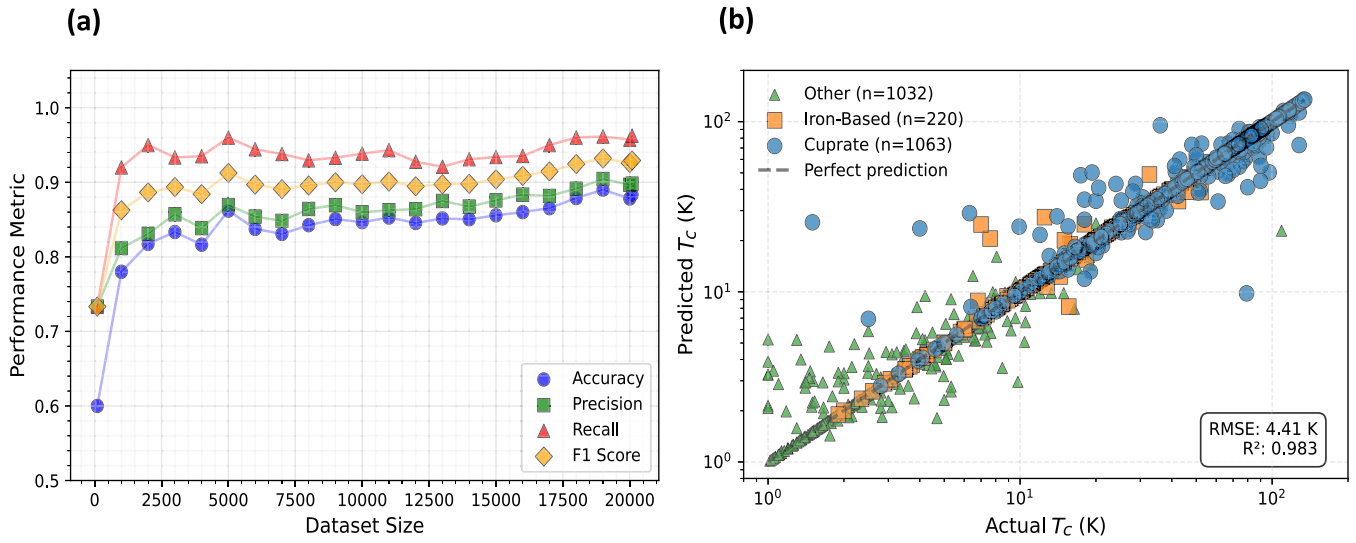

FIG. 2. Random forest performance evaluation. (a) RF classifier performance vs training data set size. (b) RF regressor predicted vs actual T_c on log scale ($n = 2315$). Materials: cuprates (blue), iron-based (orange), and others (green). RMSE = 4.41 K; $R^2 = 0.983$.

components. For this study, descriptors were expanded through mathematical operations

$$\hat{\mathcal{H}} = \left\{ \begin{array}{c} \psi_1 + \psi_2,\ \psi_1 - \psi_2,\ |\psi_1 - \psi_2|,\ \psi_1 \cdot \psi_2, \\ \frac{\psi_1}{\psi_2},\ \exp(\psi_1),\ \exp(-\psi_1),\ |\psi_1|,\ \psi_1^{-1},\ \psi_1^2,\ \psi_1^3,\ \sqrt{\psi_1},\ \sqrt[3]{\psi_1},\ \ln(\psi_1) \end{array} \right\}. \tag{2}$$

This operator set follows the SISSO++ default, which emphasizes operators common in materials science relationships (power laws, exponentials, and logarithms). Hyperbolic functions, while not explicitly prohibited, are excluded because their bounded output ranges tend to produce numerically problematic expressions in SISSO's recursive descriptor construction.

Hyperparameters were set as follows: n_sis_select = 100, n_residual = 10, max_rung = 2, and max_feat_cross_correlation = 1.0. The algorithm explored descriptor dimensions from 1 to 4, with the optimal three-dimensional model selected based on jackknife cross validation convergence check [48]. Model evaluation utilized 100 cycles of 5% jackknife resampling to ensure reliable estimation.

III. RESULTS AND DISCUSSIONS

A. Feature selection with random forest

The results of RFC and RFR are summarized in Fig. 2. In Fig. 2(a), we have demonstrated that the learning curve of RFC performance metrics evolve as the training data set size increases from 100 to 20 087. From 100 to 5000 samples RFC showed rapid improvement where all metrics jump significantly (accuracy rises from 0.70 to 0.85), followed by a plateau where performance stabilizes around 0.88–0.94 with diminishing returns from additional data. Notably, recall consistently performs best at 0.94–0.95, while precision and F1 score cluster around 0.89–0.92. For detailed information about the RFC implementation and hyperparameters, please refer to the Supplemental Material [26]. In Fig. 2(b), We have demonstrated robust predictive accuracy with $R^2 = 0.983$ and RMSE = 4.41 K for RFR across the entire T_c range spanning from 1 to 250 K. The actual vs predicted T_c parity plot reveals excellent agreement along the diagonal, with materials categorized by type: cuprates ($n = 1063$), iron-based ($n = 220$), and others ($n = 1032$). Notably, the model performs consistently accurate across all superconductor families, though slight systematic deviations appear for cuprates at intermediate T_c values (20–50 K) and some iron-based superconductors show larger scatter, implying insufficient description of their complex electronic structures with solely atomic properties.

Figure 3 displayed the distinct patterns in feature importance between RFC and RFR models. Feature importance analysis reveals electronegativity-related features dominate RFR rankings, with average deviation of electronegativity (avg_dev electronegativity) showing the highest importance (approximately 0.075), followed by mode melting point (MeltingT) and average deviation of ground state volume per atom (avg_dev GSvolume_pa). The RFC shows more balanced importance distribution, with the average deviation of numbers of unfilled orbital (avg_dev NUnfilled) leading but with reduced dominance (approximately 0.026). Features related to d electrons and unfilled orbitals appear consistently in both models' top 30 features, aligning with known physics of conventional superconductivity. Then 30 features with highest feature importance from RF analysis (without double counting overlap features) are preselected to be used as primary features of the SISSO model.

B. SISSO model for superconducting transition temperature

The 15 most important features were extracted separately from both the RFR and RFC models, yielding 25 unique

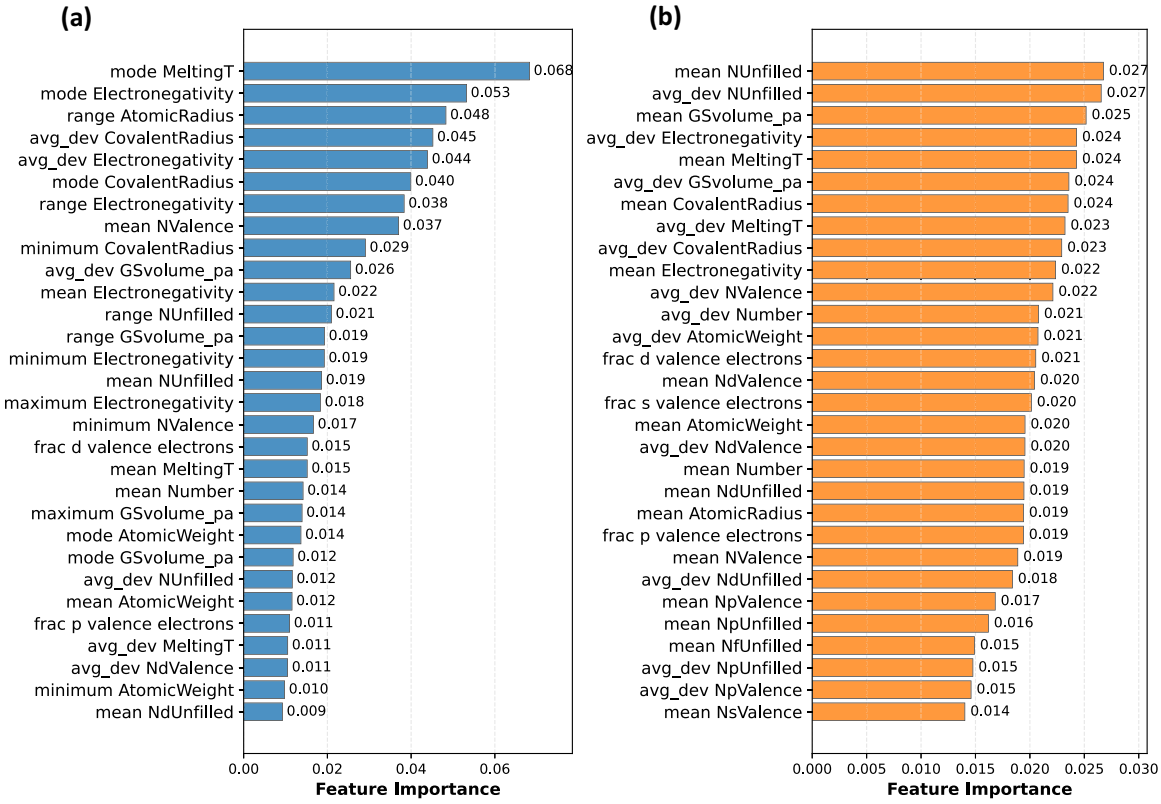

FIG. 3. Normalized feature importance from random forest models. Top 30 most important features identified by (a) random forest regressor and (b) random forest classifier models. Key features include average deviation of electronegativity, melting temperature modes, covalent radius variations, and electronic properties. Feature importance values are normalized (sum to 1.0).

features after accounting for overlaps. These were combined with 17 calculated bulk and thermodynamic property features, resulting in the primary feature set detailed in Supplemental Table I (Supplemental Material [26]); fundamental constants (e.g., π, e) are not included as explicit primary features or operators—they are implicitly encoded in the units of primary features (e.g., E_F in eV) and any remaining constant prefactors are expected to be absorbed into the fitted coefficients. Using this comprehensive set, the SISSO algorithm was employed to identify optimal descriptors for predicting the superconducting T_c. SISSO explored multidimensional descriptor spaces (with dimensions ranging from one to four) to balance predictive accuracy and model interpretability. After performing 100 cycles of jackknife resampling (with a 5% exclusion rate per cycle), the evaluation of model dimensions, Fig. 4(a), revealed that increasing complexity provides modest improvements in performance, but the four-dimensional model showed signs of overfitting with significantly worse performance on outlier test cases. Thus a three-dimensional model was adopted as it provides the optimal balance between accuracy and generalizability. As shown in Fig. 4(b), this model achieved robust predictive performance, with an RMSE of 0.088, MAE of 0.069, and $R^2 = 0.778$. To investigate how prediction error translates to T_c, the average factor difference (AFD),

$$\text{AFD} = 10^x,$$

$$\text{where} \quad x = \left(\frac{1}{n}\right)\sum_i^n \left|\log_{10}(T_{c,i}) - \log_{10}\left(T_{c,i}^{\text{pred}}\right)\right|, \qquad (3)$$

is calculated. AFD values close to 1.0 indicate high accuracy; AFD of 1.173 indicates predictions that are generally within 17.3% of the true T_c. Most predictions fall within acceptable error ranges, with only a few predictions exhibiting errors greater than 50%, suggesting the model captures the fundamental physics for most conventional superconductors.

The three-dimensional SISSO model is expressed as

$$\log_{10}(T_c) = c_0 + a_1 d_1 + a_2 d_2 + a_3 d_3, \qquad (4)$$

where

$$c_0 = 0.681, \quad a = -0.230, \quad a = 0.069, \quad a = 3.732. \qquad (5)$$

The three descriptors are as follows.

Descriptor 1 (d_1):

$$d_1 = (|\Delta(Z_{\text{unf}}) - \sigma(Z_{\text{val}})|)/(\langle Z_{\text{val}}\rangle b_{\min}). \qquad (6)$$

This descriptor combines electronic structure heterogeneity (range of unfilled orbitals) with valence electron characteristics, normalized by structural factors minimum of reciprocal length.

Descriptor 2 (d_2):

$$d_2 = |(|\langle n_d\rangle - \langle Z_{\text{unf}}\rangle|) - \Delta(\chi) - \langle Z_{\text{unf}}\rangle|. \qquad (7)$$

This descriptor captures the interplay between d-electron count, unfilled orbital availability, and electronegativity variations.

Descriptor 3 (d_3):

$$d_3 = |\Delta(\chi) - \sigma(Z_{\text{unf}})|/(\langle Z_{\text{val}}\rangle\langle\chi\rangle). \qquad (8)$$

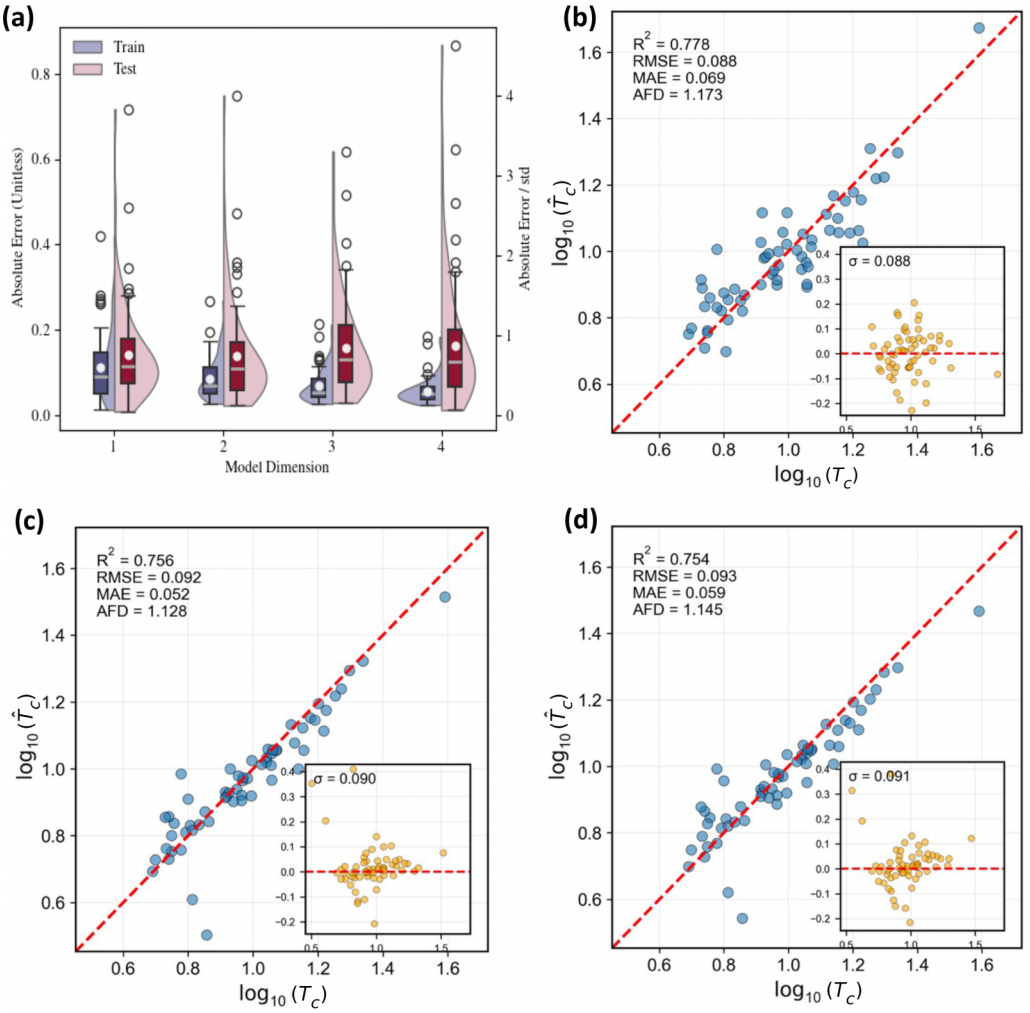

FIG. 4. Cross-validation performance comparison of machine learning models. (a) Model complexity vs performance trade-off. Violin plots comparing training and test performance across four different SISSO model dimensions. Each violin shows the distribution of prediction errors, with box plots indicating median and quartile ranges. Three-dimensional SISSO model was elected for optimal performance. Panels (b), (c), and (d) show predicted vs actual T_c and inset as residual analyses for SISSO, KRR, and GPR model, respectively.

This descriptor integrates electronegativity diversity with electronic structure uniformity, scaled by overall electronic characteristics. Here, we emphasize that interpretability in the SISSO framework arises primarily from (i) the algebraic structure of descriptors revealing which material properties and their combinations govern T_c and (ii) sensitivity analysis quantifying feature dependencies (Sec. III C), rather than from universal physical meaning of the fitted coefficients c_0, a_1, a_2, and a_3. These coefficients quantify relative descriptor importance within our data set but should not be overinterpreted as fundamental physical constants. Also, SISSO implementation permits both dimensionful and dimensionless candidate expressions during rung construction. These fitted coefficients absorb any dimensional factors, ensuring dimensional consistency of the final model with the dimensionless target $\log_{10}(T_c)$.

Comparative analysis with kernel-based methods reveals SISSO's competitive performance while maintaining interpretability. To better understand the performance of our SISSO model, we compared our model with kernel ridge regression (KRR) and Gaussian process regression (GPR). See the Supplemental Material [26] for comprehensive details on KRR and GPR configuration and training procedures. As demonstrated in Figs. 4(c) and 4(d), the performance of three models is generally comparable, with SISSO predictive performance (RMSE $= 0.088$, $R^2 = 0.778$) compared to KRR (RMSE $= 0.092$, $R^2 = 0.756$) and GPR (RMSE $= 0.093$, $R^2 = 0.754$), despite the latter providing inherent uncertainty quantification. By comparing the GPR uncertainty analysis Supplemental Fig. 2 in the Supplemental Material [26] with Fig. 4(a), it is apparent that SISSO maintains robust accuracy even in high-uncertainty regions where probabilistic methods struggle, with residuals showing random scatter around zero ($\sigma = 0.088$) and no systematic bias across the prediction range. Notably, the SISSO model achieved such accuracy by selecting only nine primary features.

Despite marginally lower AFD than KRR/GPR, a key advantage of using SISSO over interpolative methods such as KRR and GPR is that the resulting models allow for a qualitative inspection of the underlying mechanisms. The current SISSO accuracy is suitable for material screening applications, providing competitive performance compared to other

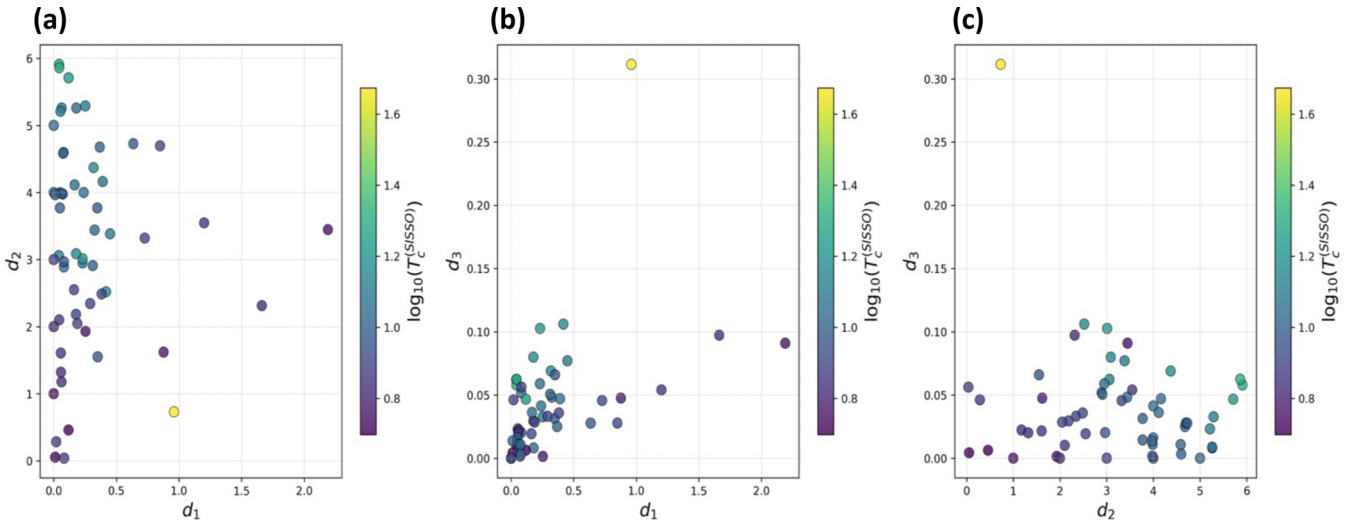

FIG. 5. Three-dimensional descriptor space analysis. Scatter plots showing the distribution of materials in the space defined by the SISSO descriptors. (a) (d_1, d_2), (b) (d_1, d_3), and (c) (d_2, d_3). Color coding represents critical temperature values (purple = low T_c; yellow = high T_c). T_c of materials are mostly controlled by d_2 and d_3. Descriptor d_1 providing only a minor correction.

machine learning approaches while maintaining high interpretability. From Fig. 5, we can see that the T_c of materials are mostly controlled by d_2 and d_3, with descriptor d_1 providing only a minor correction. Furthermore, some primary features such as Z_{unf} enter all descriptors and lower all descriptors and $\Delta(\chi)$ enter both d_2 and d_3, but with contrasting trends, i.e., $\Delta(\chi)$ lowers d_2 but increases d_3. To accelerate the exploration of materials space, one must first be able to disentangle the contradicting contributions of the involved primary features.

C. Sensitivity analysis and extraction of physical relevance

In order to extract the physical relevance and interpret the model, we employed the SHAP (SHapley Additive exPlanations), LIME (Local Interpretable Model-agnostic Explanations), and Sobol sensitivity analysis to provide detailed insights into how individual features and descriptors contribute to the SISSO model predictions. SHAP [49] leverages Shapley values from cooperative game theory and attributes the model's output for a specific prediction to each feature, taking into account all possible feature value combinations to provide local interpretablility. Similarly, LIME [50] offers complementary local interpretability by generating approximations within defined neighborhoods around individual predictions, providing insight into model behavior when averaged over all instances. The Sobol indices are calculated using the SALib package implemented by Herman and Usher [51,52]. Sobol sensitivity analysis quantifies how input features contribute to the variance of $\log_{10}(T_c)$ predictions. The first-order index S_i measures the proportion of output variance attributable to feature x_i alone, while the total-order index $S_{T,i}$ captures both main effects and all interactions involving x_i. Values range from 0 (no influence) to 1 [complete determination of $\log_{10}(T_c)$]. When $S_{T,i} > S_i$, significant interaction effects exist between x_i and other features, with the difference $(S_{T,i} - S_i)$ quantifying the interaction contribution. For example, Fig. 6(a) compares the different sensitivity metrics by treating each feature as independent; $S_i = 0.76$ for $\langle Z_{\text{val}} \rangle$ indicates it accounts for 76% of $\log_{10}(T_c)$ variance through main effects alone. Small $S_{T,i}$ values (approaching 0) suggest features could be removed without compromising model performance. Refer to the Supplemental Material [26] for

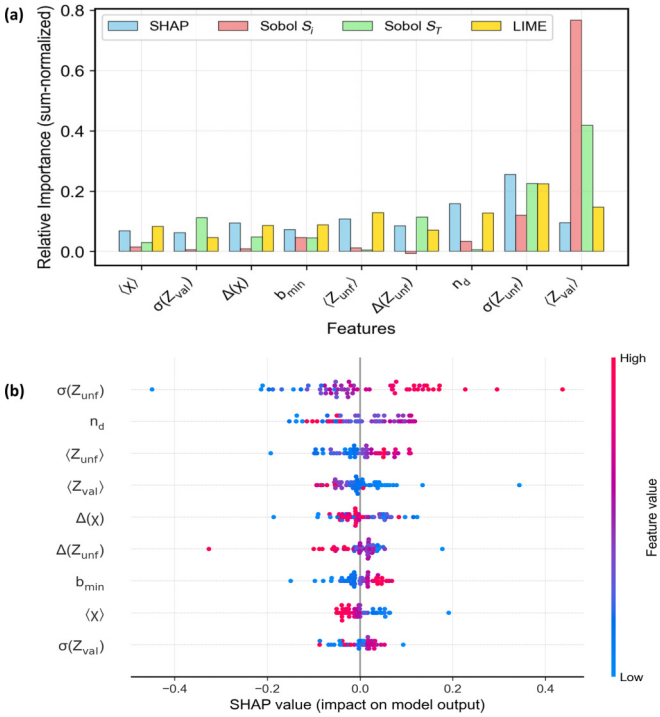

FIG. 6. Feature sensitivity comparison (independent). (a) Normalized feature importance rankings from four different interpretability methods: SHAP (blue), Sobol S_i (red), Sobol S_T (green), and LIME (yellow) for key material descriptors. (b) SHAP feature impact analysis. Each point represents a material, with position indicating SHAP value (impact on model output) and color representing feature value (blue = low; red = high).

detailed methodologies of SOBOL, SHAP, and LIME, respectively.

The analysis reveals significant heterogeneity in feature importance across different materials and critical temperature ranges. As shown in Fig. 6(b), SHAP summary plot demonstrates that the average deviation of the number of unfilled orbitals $\sigma(Z_{\text{unf}})$ consistently exhibits the highest impact to $\log_{10}(T_c)$ across all materials, with SHAP values ranging from -0.4 to $+0.4$. This feature shows a clear positive correlation with higher T_c, confirming its role as the primary electronic descriptor for conventional superconductivity. $\langle Z_{\text{val}} \rangle$ shows negative correlation with output, suggesting higher values of this parameter may lead to lower predicted critical temperatures. Range electronegativity shows positive but modest correlation, indicating its role as a moderating factor rather than primary driver. The relative contribution analysis reveals distinct patterns among the three SISSO descriptors; d_2 shows the highest median contribution ($\approx$54%) with extreme variability, indicating its dominant but context-dependent role. Also, d_3 exhibits the second highest contribution ($\approx$31%), while d_1 provides more modest but consistent contributions across all materials.

In Fig. 7 , we have illustrated the SHAP dependence plots for most important features. Across all three plots, the interplay between electronic descriptors reveals a sophisticated multidimensional optimization landscape for superconductivity. At first glance at Fig. 7(a), the interplay of $\Delta(Z_{\text{unf}})$ and $\sigma(Z_{\text{unf}})$ seems to be trivial since they are typically proportionate; however, it reveals that electronic heterogeneity itself is a design principle, with sharp transition around $\sigma(Z_{\text{unf}}) \approx$ 1.5–2.0 and materials showing strongly positive SHAP values ($+0.1$ to $+0.4$) only when $\sigma(Z_{\text{unf}}) > 2.0$, suggesting that optimal superconductors are not electronically homogeneous but rather benefit from controlled disorder that creates complementary electronic environments for enhanced pairing mechanisms. These trends are aligned with Anderson's theorem [53], stating homogeneity is necessary in conventional (BCS) superconductors to make them robust with respect to (nonmagnetic) disorder and to maintain electronic coherence for phonon-mediated pairing. As a result, most elemental and simple alloy superconductors display relatively low T_c compared to unconventional families, while outliers like hydride superconductors exhibiting record-high T_c ($>$200 K) at megabar pressures bypasses these limitations through ultrahigh-frequency phonons ($>$20 THz) arising from light hydrogen atoms and exceptionally strong electron-phonon coupling [54]. Despite using only conventional superconductors in our data set, these findings extend to unconventional systems. Substantial evidence indicates that local heterogeneity and inhomogeneity in the electronic environment can locally enhance the DOS near the Fermi level and influence superconductivity, especially in cuprates and iron-based superconductors. Experiments show that superconductivity often emerges in a percolative manner, with spatially varying gap values and domains, especially near critical doping points [55,56]. Cuprate superconductors exemplify how electronic heterogeneity can enhance superconducting properties, exhibiting high values of both $\sigma(Z_{\text{unf}})$ and $\Delta(Z_{\text{unf}})$ that correlate with high T_c. The fundamental mechanism involves orbital differences between copper atoms (with one unfilled

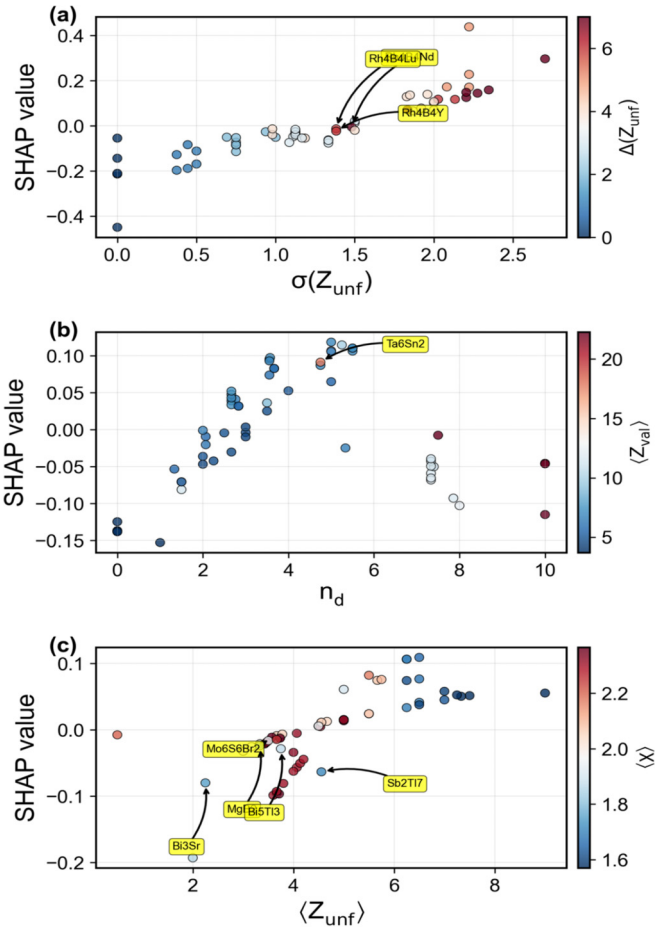

FIG. 7. SHAP dependency analysis. (a) SHAP values vs $\sigma(Z_{\text{unf}})$ colored by $\Delta(Z_{\text{unf}})$, revealing positive correlation and interaction effects; (b) SHAP values vs n_d colored by $\langle Z_{\text{val}} \rangle$, showing optimal performance around five d electrons; (c) SHAP values vs $\langle Z_{\text{unf}} \rangle$, colored by $\langle \chi \rangle$, demonstrating the importance of moderate unfilled orbital heterogeneity. Outliers are annotated from left to right including (a) Rh_4B_4Lu, Rh_4B_4Y, and Rh_4B_4Nd, (b) Ta_6Sn_2, and (c) Bi_3Sr, MgB_2, $Mo_6S_6Br_2$, Bi_5Tl_3, and Sb_2Tl_7.

$3d$ orbital) and oxygen atoms (with filled p orbitals), creating high $\sigma(Z_{\text{unf}})$ values which enables the d-wave pairing symmetry characteristic of cuprates, where spin fluctuations rather than lattice vibrations mediate pairing, with effective interactions occurring between neighboring copper orbitals and surrounding oxygen orbitals [57]. The charge transfer (CT) between Cu and O sites [55] creates $\Delta(Z_{\text{unf}})$ variation with doped holes predominantly occupying the oxygen sublattice that enhances pairing through Zhang-Rice singlet formation [57]. Experimental evidence directly links this heterogeneity to higher transition temperatures, showing that maximum T_c increases as hole content shifts from copper to planar oxygen orbitals, demonstrating that optimized electronic heterogeneity drives superconducting enhancement through improved charge redistribution [58]. High $\sigma(Z_{\text{unf}})$ within a structure also implies some atomic sites act as electron donors while others act as acceptors, which is foundational in systems displaying strong CT character, facilitating CT between layers or sublattices in complex superconductors [55,59]. Also,

iron-based superconductors demonstrate intermediate heterogeneity levels through complex multiorbital properties. Their electronic structure involves five Fe 3*d* orbitals with different filling patterns, generating moderate $\sigma(Z_{\text{unf}})$ values through orbital multiplicity and creating multiple pockets in the Fermi surface. These systems exhibit orbital-selective superconductivity where different orbitals contribute differently to pairing—some becoming "coherence-suppressed" while others dominate—creating a $\Delta(Z_{\text{unf}})$ variation that plays a key role in the more strongly correlated iron-based superconductors [60]. On the other hand, the $s\pm$-wave pairing symmetry specifically requires heterogeneity between electron and hole pockets, with Fermi surface nesting inducing strong pairing when enhanced simultaneously on nearly nested pockets, showing how optimized $\sigma(Z_{\text{unf}})$ enhances interband pairing mechanisms [61]. This structural flexibility demonstrates that controlled heterogeneity optimization can enhance properties, as extending from single-band to effective multiband models allows for orbital-dependent and orbital-selective pairing, illustrating how tuned $\Delta(Z_{\text{unf}})$ distributions enable multiband superconducting enhancement [62]. In contrast, extreme heterogeneity [$\sigma(Z_{\text{unf}}) \approx 4.0$–$8.0$] and highly localized *f* electrons ($n_f > 10$) coexist with itinerant conduction electrons ($n_c \approx 0$–2, $c = d$ if electrons are from *d* orbital) in heavy fermion superconductors involving Kondo coupling between localized *f* moments and conduction electrons, where competition between Kondo screening and RKKY magnetic interactions creates orbital-selective hybridization between vastly different electronic states. This *f*-*c* hybridization between further enhances $\sigma(Z_{\text{unf}})$ values, but excessive electronic heterogeneity typically suppresses rather than enhances T_c, explaining why heavy fermion superconductors generally exhibit much lower T_c values compared to other unconventional superconductors despite their strong electronic correlations [63,64]. Therefore, we must acknowledge that $\sigma(Z_{\text{unf}})$ and $\Delta(Z_{\text{unf}})$ could serve as valuable, but not universal design guidelines that must be integrated with other electronic, chemical, and structural descriptors while recognizing that a different superconductor family might require tailored optimization within material-specific electronic heterogeneity windows.

Figure 7(b) shows a clear inverted U-shaped relationship where materials with approximately 4–5 *d* electrons exhibit the highest positive SHAP values (approximately +0.1). This demonstrates that optimal superconducting performance requires synergistic coordination between average *d*-electron count (n_d) and total valence electron density, where materials achieve peak enhancement only when $n_d \approx 4$–5 *d* electrons coincide with high mean valence electrons ($\langle Z_{\text{val}} \rangle > 15$), indicating that superconductivity is maximized when both optimal *d*-band filling and a sufficiently high total valence electron density are achieved simultaneously; one without the other results in weak or absent superconductivity—a principle borne out in both experiment (Nb_3Sn, MgB_2) and machine learning approaches [43,59,65], and originally observed as "Matthias' rules" [66], which is largely supported for conventional and near-conventional superconductors. Notably, this pattern differs fundamentally from unconventional superconductors where the $\langle Z_{\text{val}} \rangle - n_d$ interplay operates through entirely different mechanisms. In cuprates, optimal superconductivity typically occurs near the border of a Mott insulating (half-filled *d*-band) regime, where doping tunes both n_d and $\langle Z_{\text{val}} \rangle$ to a region favorable for pairing via superexchange [67,68]. Iron-based superconductors present yet another paradigm, where the multiorbital nature of Fe 3*d* electrons means that $\langle Z_{\text{val}} \rangle$ and n_d jointly tune Fermi surface nesting and spin fluctuations [69], with optimal superconductivity occurring in an intermediate regime between localized and itinerant *d*-electron behavior—too high or too low in either direction suppresses superconductivity through magnetic ordering or electron localization [70], as indicated by the inverted U-shaped pattern. Heavy fermion superconductors add further complexity, where $\langle Z_{\text{val}} \rangle$ includes contributions from both itinerant *d* electrons and localized *f* electrons, with their hybridization creating massive quasiparticles; the interplay determines not just carrier density but the degree of *f*-*d* hybridization that enables unconventional pairing through magnetic or Kondo-mediated interactions [71]. This diversity underscores that, while the SHAP analysis captures the electron-phonon coupling optimization in BCS-type superconductors through the Matthias rules, each class of unconventional superconductors follows distinct design principles where n_d and $\langle Z_{\text{val}} \rangle$ influence fundamentally different microscopic mechanisms—from magnetic correlations to orbital selectivity to heavy fermion hybridization.

Figure 7(c) extends this understanding by showing that electronic availability must be coupled appropriately to shape the electronic environment conducive to Cooper pair formation and CT. For conventional superconductors, high unfilled orbital counts ($\langle Z_{\text{unf}} \rangle > 6$) provide necessary "parking spaces" for Cooper pairs, but only when modulated by intermediate electronegativity values ($\langle \chi \rangle \approx 1.8$–$2.0$) that ensure these orbitals remain electronically accessible; lower $\langle \chi \rangle$ supports delocalized metallic bonding conducive to superconducting behaviors, while overly high $\langle \chi \rangle$ leads to electron localization and diminished orbital utilization. Cuprates leverage high $\langle Z_{\text{unf}} \rangle$ from partially filled Cu *d* orbitals combined with mixed Cu-O electronegativities to create the charge-transfer physics and electronic correlations essential for their high-T_c behavior [72,73], while iron-based superconductors utilize high $\langle Z_{\text{unf}} \rangle$ from Fe *d* orbitals with moderate χ to balance metallicity and magnetism, enabling spin-fluctuation-mediated pairing, and heavy fermion systems employ partially filled *f* orbitals (high $\langle Z_{\text{unf}} \rangle$) with carefully tuned electronegativity to stabilize the coexistence of localized and itinerant electrons necessary for Kondo physics and exotic pairing [74,75]. Across all families, optimal superconductivity emerges not from maximizing either parameter alone, but from finding the precise balance where sufficient orbital availability ($\langle Z_{\text{unf}} \rangle$) meets the right degree of electron delocalization ($\langle \chi \rangle$), with this "Goldilocks zone" determining whether pairing occurs through conventional electron-phonon coupling or more exotic mechanisms involving spin, charge, or orbital fluctuations.

Several outliers are visually apparent in Fig. 7, where certain correlated secondary features (color bar) of materials deviate from the expected clusters in SHAP dependence plots. To systematically confirm and characterize these outliers, we employed K-means clustering on the feature-SHAP value space, which validated the visual observations and

revealed that these materials represent cases where compositional descriptors struggle, despite SISSO's generally strong performance. See the Supplemental Material [26] for detailed analysis and methodology.

The SOBOL sensitivity analysis provides a variance-based assessment complementing the SHAP analysis with quantitative measures of individual and interaction effects. The combined analysis reveals a clear feature hierarchy; while electronic structure features (d-valence electrons, unfilled orbitals) dominate the variance contribution, chemical bonding characteristics (electronegativity variations) provide secondary but significant effects. Finally, structural parameters contribute through interactions rather than direct effects. Together, these interplays demonstrate that the emergence of superconductivity requires simultaneously optimized d-band filling, sufficient unfilled orbital availability, balanced electronegativity for electronic mobility, and designed heterogeneity for multiple pairing pathways.

D. Connection between SISSO-identified features and theoretical frameworks

In this section we discuss the mapping between data-driven features and microscopic physics of conventional superconductors. We first revisit the BCS theory and Eliashberg-Migdal formalism; then we examine the influences of the most important SISSO-identified features in the following order: (i) Z_{unf}, (ii) Z_{val}, (iii) n_d, and (iv) χ.

1. Microscopic theories of conventional superconductivity

Assuming weak electron-phonon coupling ($\lambda \ll 1$) and an instantaneous, energy-independent pairing interaction, the BCS [2,64] gap equation took the simple form

$$\Delta_{\mathbf{k}} = \frac{1}{2}\sum_{\mathbf{k}'} U_{\mathbf{k},\mathbf{k}'}\frac{\Delta_{\mathbf{k}'}}{E_{\mathbf{k}'}}\tanh\left(\frac{E_{\mathbf{k}'}}{2k_{\text{B}}T}\right), \tag{9}$$

where Δ is the superconducting energy gap, $E_{\mathbf{k}'} = \sqrt{\xi_{\mathbf{k}}^2 + \Delta_{\mathbf{k}'}^2}$ is the quasiparticle excitation energy at wave vector $\mathbf{k}'$, and effective pairing interaction $U_{\boldsymbol{k},\boldsymbol{k}'} = -V_0$ is a constant if $E_{\text{F}} \leqslant \epsilon_{\mathbf{k}} \leqslant E_{\text{F}} + \hbar\omega_{\text{D}}$ and zero otherwise. ω_{D} is the Debye frequency and T is the absolute temperature. This yielded the BCS relation

$$2\Delta_0 \approx 3.5k_{\text{B}}T_c \tag{10}$$

and

$$T_c \propto \omega_{\text{D}}\exp\left(-\frac{1}{N_{\text{F}}V_0}\right), \tag{11}$$

where N_{F} is the DOS at the Fermi level. BCS theory treated phonons only through the Debye cutoff ω_{D}, without considering the detailed phonon spectrum or retardation effects [76]. To properly include retardation effects and frequency-dependent interactions, electron-phonon coupling spectral function $\alpha^2F(\omega)$ is introduced in the Eliashberg equation [77], which is later reformulated using Nambu-Gor'kov formalism [78,79] and Migdal's theorem [80] into

$$Z(\mathbf{k}, i\omega_n) = 1 + \frac{\pi T}{N_{\text{F}}\omega_n}\sum_{\mathbf{k}'n'}\frac{\omega'_n}{\sqrt{\omega_n'^2 + \Delta^2(\mathbf{k}', i\omega'_n)}} \times \lambda(\mathbf{k}, \mathbf{k}', n-n')\delta(\epsilon_{\mathbf{k}'}), \tag{12}$$

$$Z(\mathbf{k}, i\omega_n)\Delta(\mathbf{k}, i\omega_n) = \frac{\pi T}{N_{\text{F}}}\sum_{\mathbf{k}'n'}\frac{\Delta(\mathbf{k}', i\omega_n')}{\sqrt{\omega_n'^2 + \Delta^2(\mathbf{k}', i\omega_n')}} \times [\lambda(\mathbf{k}, \mathbf{k}', n-n') - N_{\text{F}}U(\mathbf{k}-\mathbf{k}')]\delta(\epsilon_{\mathbf{k}'}). \tag{13}$$

In Eq. (12), Z denotes the renormalization function, $i\omega_n = i(2n+1)$ are the Matsubara frequencies, and $\lambda(\mathbf{k}, \mathbf{k}', n-n')$ is the anisotropic electron-phonon coupling matrix given by

$$\lambda(\mathbf{k}, \mathbf{k}', n-n') = \int_0^\infty d\omega \frac{2\omega}{(\omega_n - \omega'_n)^2 + \omega_n}\alpha^2F(\mathbf{k}, \mathbf{k}', \omega), \tag{14}$$

$$\alpha^2F(\omega) = 1/N_{\text{F}}\sum_{\mathbf{k},\mathbf{k}',\nu}\left|g^{\nu}_{\mathbf{k},\mathbf{k}'}\right|^2\delta(\epsilon_{\mathbf{k}})\delta(\epsilon_{\mathbf{k}'})\delta(\omega - \omega_{\mathbf{q}\nu}), \tag{15}$$

where $g^{\nu}_{\mathbf{k},\mathbf{k}'}$ is the electron-phonon matrix element and $\omega_{q\nu}$ is the phonon frequency for branch ν at wave vector $\mathbf{q} = \mathbf{k} - \mathbf{k}'$. For practical calculations McMillan [81] and Allen and Dynes [82] derived an approximate solution to the Eliashberg-Migdal equations:

$$T_c = \frac{f_1 f_2 \omega_{\log}}{1.2}\exp\left[-\frac{1.04(1+\lambda)}{\lambda - \mu^*(1+0.62\lambda)}\right], \tag{16}$$

where $\omega_{\log}$ is the log average of the phonon frequencies and f_1 and f_2 are factors depending on λ and the Morel-Anderson Coulomb pseudopotential [83] μ^*:

$$\lambda = N_{\text{F}}\langle I^2\rangle/M\langle\omega^2\rangle, \tag{17}$$

$$\mu^* = \frac{\mu}{1 + \mu\ln(E_{\text{F}}/\omega_{\text{D}})}, \tag{18}$$

respectively. $\langle I^2\rangle$ is a Fermi-surface average of the squared modulus of electron-phonon matrix elements, i.e., $\langle|g|^2\rangle$.

2. Orbital heterogeneity and multiband effects

Figure 6(b) and Fig. 7(a) demonstrated that $\sigma(Z_{\text{unf}})$ emerged as the principle component in the SISSO model; it directly impacts the electron-phonon coupling through multiband effects in such a manner that materials with high $\sigma(Z_{\text{unf}})$, different atomic sites contribute distinct orbital characters to the Fermi surface, creating multiple coupling channels $\lambda_{\text{total}} = \sum_i \omega_i\lambda_i$, where ω_i are Fermi surface weights from band i. This heterogeneity enhances the total coupling by allowing different bands to optimize different aspects of the pairing interaction. High orbital heterogeneity prevents the saturation of λ that occurs in single-band systems when $N_{\text{F}}V_0$ in Eq. (11) approaches unity [84]. The classic example is MgB_2, where two distinct bands (σ and π) with differing electron-phonon coupling strengths collaborate, leading to a high T_c for a phonon-mediated superconductor [85,86], explaining why $\sigma(Z_{\text{unf}})$ emerges as the primary feature in our SISSO model.

3. Valence electrons and Coulomb screening

While Z_{unf} and Z_{val} features are complementary—two ways of counting electrons relative to a closed shell—they influence superconductivity through different mechanisms. Z_{unf} primarily determines the type of orbitals are at the Fermi level and Z_{val} on the other hand determines the density of electrons participate in screening. Within the BCS framework, the formation of Cooper pair has competing effects between the attractive interaction from electron-phonon coupling and the repulsive Coulomb repulsion. Instead of bare Coulomb interaction, electrons experience a screened interaction that decays exponentially over the Thomas-Fermi length [87] (λ_{TF}), where relation $\lambda_{\text{TF}}^2 \propto \langle Z_{\text{val}} \rangle^{-1/3}$ holds at low temperature. This Thomas-Fermi screening is crucial for conventional superconductivity because it reduces the repulsion, making it easier for attractive phonon-mediated interaction to overcome and form Cooper pairs. Also, the short-range nature of λ_{TF}, typically 1 Å to 10 Å, causes Coulomb repulsion to affect only electrons that are closely packed, while Cooper pairs have a much larger coherence length which normally exceed 100 Å in conventional superconductors. This screening effect is incorporated through μ estimation in Eq. (16). As a result, higher $\langle Z_{\text{val}} \rangle$ leads to a stronger screening (shorter λ_{TF}), produces a smaller μ and thus a smaller μ^*, and ultimately a higher T_c according to Eq. (16).

4. d-electron count and density of states

Figure 7(b) illustrated that T_c receives peak enhancement when n_d is near half filled; this filling controls where the Fermi level lies relative to the Van Hove singularity (VHS) in DOS. When the d-electron count leads to the Fermi level being near or at VHS, the system experiences a peak in the DOS dominated by d-orbital bands. From Eq. (11), this peak in N_{F} increases the number of states available for Cooper pairing, thus strengthening superconductivity and enhancing T_c [88]. The VHS-induced DOS peaks can also lead to unconventional superconducting states, such as d-wave or chiral pairing symmetries, beyond conventional phonon-mediated BCS-type superconductivity, and several studies have directly demonstrated that a half-filled or near half-filled valence d-orbital often places the E_{F} near VHS in correlated electron materials, such as kagome metals [89], cuprates [90], and nickelates [91,92] superconductors. Additionally, the electron-phonon matrix element for d orbitals scales as

$$\langle I^2 \rangle_d \propto \frac{1}{r_d^3}, \tag{19}$$

where r_d is the d-orbital radius. Partial d-band filling provides optimal orbital extension, balancing between localization (small r_d, large $\langle I^2 \rangle_d$) and metallicity (extended orbitals, good conduction) [93].

5. Electronegativity and phonon spectrum

While the n_d is crucial in controlling the Fermi level relative to band singularities, electronegativities between constituent atoms also serve as the fundamental physicochemical factor influencing the DOS and superconductivity. Higher electronegativity leads to increased electron localization, which narrows the bandwidth W [94] according to $W(\langle \chi \rangle) = W^0 \exp(-\beta \langle \chi \rangle)$, where $\beta \approx 0.3$–0.5 Å^{-1}, thereby enhancing the N_{F} as $N_{\text{F}} \propto 1/W$. This bandwidth narrowing effect competes with band center shifts $E_c(\langle \chi \rangle) = E_c^o - \gamma \langle \chi \rangle$, where $\gamma \approx 1$–2 eV per unit electronegativity, which can move the Fermi level away from optimal positions in the band [95]. The electron-phonon coupling strength is also affected through the matrix element $\langle I2 \rangle$, which depends on the spatial extent of electronic wave functions that contract with increasing $\langle \chi \rangle$ as $\psi(r) \propto \exp(-\alpha(\chi)\mathbf{r})$, creating a complex optimization problem for maximizing Eq. (17) [96]. Additionally, $\langle \chi \rangle$ influences μ^* through its effect on electronic screening, with higher electronegativity reducing polarizability and thereby increasing μ^*, which suppresses T_c according to Eq. (16). Empirical analysis of conventional superconductors reveals an optimal range of $\langle \chi \rangle \approx 1.7$–$2.2$ on the Pauling scale, exemplified by high-T_c materials like MgB_2 ($\langle \chi \rangle = 1.80$, $T_c = 39$ K) and A15 compounds such as Nb_3Sn($\langle \chi \rangle = 1.69$, $T_c = 18$ K), where this intermediate electronegativity provides sufficient $N(E_{\text{F}})$ without excessive electron localization, moderate electron-phonon coupling, and adequate Coulomb screening [66,97].

IV. CONCLUSION

This work demonstrates successful integration of RF screening with SISSO symbolic regression for discovering interpretable superconductivity descriptors. The two-stage approach addresses complementary challenges: RF handles high-dimensional feature selection with exceptional predictive power ($R^2 = 0.983$), while SISSO provides interpretable expressions capturing essential physics.

The 0.3 K threshold for superconductor classification, motivated by the Kohn-Luttinger theorem, provides physically meaningful distinction between practical superconductors and materials with theoretical instabilities and the RFC's high performance (88.8% accuracy) validates this threshold choice. RFR's consistent performance across three orders of magnitude and different material families demonstrates robustness of atomic descriptors for T_c prediction. Slight deviations for cuprates and iron-based materials reflect additional complexity beyond electron-phonon coupling, suggesting our conventional superconductor-optimized approach captures some universal features.

SISSO's competitive performance against KRR/GPR (SISSO AFD = 1.173 vs KRR 1.128, GPR 1.145) while providing interpretability represents well balanced accuracy and interpretability. The analytical expressions enable extrapolation and provide design insights impossible with black-box models. Multimethod sensitivity analysis reveals complementary perspectives. SHAP and LIME identifies region-specific behaviors and SOBOL quantifies global variance contributions. Agreement across methods strengthens confidence in identified relationships.

SHAP analysis reveals that the synergistic interplay of four key electronic descriptors, Z_{unf}, Z_{val}, χ, and n_d, is crucial to enhance T_c. Rather than optimizing individual parameters, the analysis demonstrates that these features must be collectively balanced to achieve optimal superconductivity. The identified design principles indicate that effective superconductors require (1) controlled electronic heterogeneity

$[\sigma(Z_{\text{unf}}) > 2.0]$ that creates complementary electronic environments for enhanced pairing, (2) optimal d-electron filling ($n_d \approx 4$–5) combined with high valence electron density ($\langle Z_{\text{val}} \rangle > 15$) to balance metallic conductivity with pairing interactions, and (3) sufficient orbital availability ($\langle Z_{\text{unf}} \rangle > 6$) modulated by intermediate electronegativity ($\langle \chi \rangle \approx 1.8$–$2.0$) to maintain electronic accessibility while preserving metallic character, creating a multidimensional optimization landscape where superconductivity emerges at the intersection of controlled heterogeneity, optimal orbital filling, and balanced chemical bonding.

Comparison with purely data-driven approaches highlights SISSO's value. While RF achieves higher R^2 through complex nonlinear decision boundaries, SISSO's simple analytical form enables physical interpretation and confident extrapolation. This interpretability-accuracy trade-off is favorable for materials discovery where understanding mechanisms is as important as prediction accuracy.

On the other hand, we must also emphasize that while the present SISSO framework provides a solid foundation and successfully captures the electronic and orbital physics governing conventional superconductivity, its application to unconventional superconductors reveals both insights and fundamental limitations. The universal importance of orbital heterogeneity $\sigma(Z_{\text{unf}})$ and optimal n_d suggests some organizing principles that transcend pairing mechanisms. However, the absence of magnetic and correlation descriptors means the model lack of capability to directly capture the essential physics of spin-fluctuation-mediated pairing, magnetic frustration effects, or the interplay between magnetism and superconductivity that defines unconventional superconductors. Future machine learning approaches to unconventional superconductivity must explicitly incorporate magnetic degrees of freedom, potentially through a hierarchical model that first screens for electronic favorability, then evaluates magnetic properties. Only by bridging the electronic and magnetic aspects of these materials can we hope to achieve predictive capability for unconventional superconductors while maintaining generalizability in model interpretation.

ACKNOWLEDGMENTS

This work received financial support from the National Key Research and Development Program of China (Grant No. 2022YFA1204100), the National Natural Science Foundation of China (Grant No. 62488201), and the CAS Superconducting Research Project (No. SCZX-0101). The authors acknowledge computational resources provided by the Max Planck Computing and Data Facility and thank the scientific computing community MS1P and fellows in the Fritz-Haber Institute for useful discussions involving FHI-aims, FHI-vibes, and SISSO software packages used in this work.

DATA AVAILABILITY

Additional supporting materials including detailed computational parameters, complete feature lists, SISSO hyperparameters, extended datasets, and supplementary analyses. Raw data from the NIMS superconductor database is publicly available at the National Institute for Materials Science repository [25]. Custom analysis scripts for RF feature selection, SISSO implementation, and sensitivity analysis calculations will be available through the corresponding authors upon reasonable request.

[1] H. Kamerlingh Onnes, The superconductivity of mercury, Commun. Phys. Lab. Univ. Leiden. Suppl. 122, 124 (1911).
[2] J. Bardeen, L. N. Cooper, and J. R. Schrieffer, Microscopic theory of superconductivity, Phys. Rev. **106**, 162 (1957).
[3] G. W. Webb, F. Marsiglio, and J. E. Hirsch, Superconductivity in the elements, alloys and simple compounds, Phys. C: Supercond. Appl. **514**, 17 (2015).
[4] C. W. Chu, L. Z. Deng, and B. Lv, Hole-doped cuprate high temperature superconductors, Phys. C: Supercond. Appl. **514**, 290 (2015).
[5] H. Hosono and K. Kuroki, Iron-based superconductors: Current status of materials and pairing mechanism, Phys. C: Supercond. Appl. **514**, 399 (2015).
[6] C. C. Chang, T. K. Chen, W. C. Lee, P. H. Lin, M. J. Wang, Y. C. Wen, P. M. Wu, and M. K. Wu, Superconductivity in Fe-chalcogenides, Phys. C: Supercond. Appl. **514**, 423 (2015).
[7] B. D. White, J. D. Thompson, and M. B. Maple, Unconventional superconductivity in heavy-fermion compounds, Phys. C: Supercond. Appl. **514**, 246 (2015).
[8] X. Zhou, W. S. Lee, M. Imada, N. Trivedi, P. Phillips, H. Kee, P. Törmä, and M. Eremets, High-temperature superconductivity, Nat. Rev. Phys. **3**, 462 (2021).
[9] D. Persaud, L. Ward, and J. Hattrick-Simpers, Reproducibility in materials informatics: Lessons from 'A general-purpose machine learning framework for predicting properties of inorganic materials,' Digit. Discov. **3**, 281 (2024).
[10] V. Gupta, A. Peltekian, W.-k. Liao, A. Choudhary, and A. Agrawal, Improving deep learning model performance under parametric constraints for materials informatics applications, Sci. Rep. **13**, 9128 (2023).
[11] J. Kong, Q. Li, J. Li, Y. Liu, and J. Zhu, Self-supervised graph neural networks for accurate prediction of néel temperature, Chin. Phys. Lett. **39**, 067503(2022).
[12] K. Choudhary and K. Garrity, Designing high$-T_c$ superconductors with BCS-inspired screening, density functional theory, and deep-learning, npj Comput. Mater. **8**, 244 (2022).
[13] T. D. Le, R. Noumeir, H. L. Quach, J. H. Kim, J. H. Kim, and H. M. Ki, Critical temperature prediction for a superconductor: A variational bayesian neural network approach, IEEE Trans. Appl. Supercond. **30**, 1 (2020).
[14] J. Zhang, K. Zhang, S. Xu, Y. Li, C. Zhong, M. Zhao, H.-J. Qiu, M. Qin, X.-D. Xiang, K. Hu, and X. Lin, An integrated machine learning model for accurate and robust prediction of superconducting critical temperature, J. Energy Chem. **78**, 232 (2023).
[15] Y. Zhang and X. Xu, Predicting the superconducting transition temperature of high-Temperature layered superconductors via

machine learning, Physica C (Amsterdam, Neth.) **595**, 1354031 (2022).

[16] L. Chen, W. Zhang, Z. Nie, S. Li, and F. Pan, Generative models for inverse design of inorganic solid materials, J. Mater. Inf. **1**, 4 (2021).

[17] Z. Li, W. T. Nash, S. P. O'Brien, Y. Qiu, and R. K. Gupta, and N. Birbilis, cardiGAN: A generative adversarial network model for design and discovery of multi principal element alloys, J. Mater. Sci. Technol. **125**, 81 (2022).

[18] J. Vybiral, E. Ahmetcik, R. H. Ouyang, S. V. Levchenko, C. Draxl, and M. Scheffler, Learning physical descriptors for materials science by compressed sensing, New J. Phys. **19**, 023017 (2017).

[19] R. H. Ouyang, S. Curtarolo, E. Ahmetcik, M. Scheffler, and L. M. Ghiringhelli, SISSO: A compressed-sensing method for identifying the best low-dimensional descriptor in an immensity of offered candidates, Phys. Rev. Mater. **2**, 083802 (2018).

[20] L. Foppa, L. M. Ghiringhelli, F. Girgsdies, M. Hashagen, P. Kube, M. Hävecker, S. J. Carey, A. Tarasov, P. Kraus, F. Rosowski, *et al.*, Materials genes of heterogeneous catalysis from clean experiments and artificial intelligence, MRS Bull. **46**, 1016 (2021).

[21] T. A. R. Purcell, M. Scheffler, L. M. Ghiringhelli, and C. Carbogno, Accelerating materials-space exploration for thermal insulators by mapping materials properties via artificial intelligence, npj Comput. Mater. **9**, 112 (2023).

[22] S. R. Xie, G. R. Stewart, J. J. Hamlin, P. J. Hirschfeld, and R. G. Hennig, Functional form of the superconducting critical temperature from machine learning, Phys. Rev. B **100**, 174513 (2019).

[23] S. R. Xie, Y. Quan, A. C. Hire, B. Deng, J. M. DeStefano, I. Salinas, U. S. Shah, L. Fanfarillo, J. Lim, J. Kim, *et al.*, Machine learning of superconducting critical temperature from Eliashberg theory, npj Comput. Mater. **8**, 14 (2022).

[24] L. Breiman, Random forests, Mach. Learn. **45**, 5 (2001).

[25] Center for Basic Research on Materials, MDR SuperCon Datasheet Ver. 240322, https://doi.org/10.48505/nims.4487.

[26] See Supplemental Material at http://link.aps.org/supplemental/10.1103/4pxk-z8ww for data set creation and data handling procedures including DFT computational setup and phonon convergence criteria (Note 1), RF hyperparameter optimization and threshold sensitivity analysis (Note 2), KRR and GPR implementations (Notes 3–4), validation on additional conventional superconductors (Note 5), SOBOL, SHAP, and LIME sensitivity analysis methodologies (Notes 6–7, 9), outlier analysis (Note 8), primary feature definitions (Supplemental Table I), feature importance rankings across thresholds (Supplemental Table II), out-of-sample validation results (Supplemental Table III), SISSO training set predictions and descriptor values (Supplemental Table IV), classification performance evaluation (Supplemental Fig. 1), threshold sensitivity analysis (Supplemental Fig. 2), and GPR ensemble prediction with uncertainty quantification (Supplemental Fig. 3), which includes Refs. [27–35].

[27] M. Esters, C. Oses, S. Divilov, H. Eckert, R. Friedrich, D. Hicks, M. J. Mehl, F. Rose, A. Smolyanyuk, A. Calzolari, *et al.*, aflow.org: A web ecosystem of databases, software and tools, Comput. Mater. Sci. **216**, 111808 (2023).

[28] M. K. Horton, P. Huck, R. X. Yang, J. M. Munro, S. Dwaraknath, A. M. Ganose, R. S. Kingsbury, M. Wen, J. X. Shen, T. S. Mathis, *et al.*, Accelerated data-driven materials science with the Materials Project, Nat. Mater. **24**, 1522 (2025).

[29] S. Gražulis, D. Chateigner, R. T. Downs, A. T. Yokochi, M. Quiros, L. Lutterotti, E. Manakova, J. Butkus, P. Moeck, and A. Le Bail, Crystallography Open Database–an open-access collection of crystal structures, J. Appl. Crystallogr. **42**, 726 (2009).

[30] J. P. Perdew, K. Burke, and M. Ernzerhof, Generalized gradient approximation made simple, Phys. Rev. Lett. **77**, 3865 (1996).

[31] W. P. Huhn and V. Blum, One-hundred-three compound band-structure benchmark of post-self-consistent spin-orbit coupling treatments in density functional theory, Phys. Rev. Mater. **1**, 033803 (2017).

[32] D. Bajusz, A. Rácz, and K. Héberger, Why is Tanimoto index an appropriate choice for fingerprint-based similarity calculations? J. Cheminform. **7**, 20 (2015).

[33] M. Kuban, S. Rigamonti, M. Scheidgen, and C. Draxl, Density-of-states similarity descriptor for unsupervised learning from materials data, Sci. Data **9**, 646 (2022).

[34] T. Head, M. Kumar, H. Nahrstaedt, G. Louppe, and I. Shcherbatyi, scikit-optimize/scikit-optimize (v0.9.0), Zenodo (2021), https://doi.org/10.5281/zenodo.5565057.

[35] F. Pedregosa, G. Varoquaux, A. Gramfort, V. Michel, B. Thirion, O. Grisel, M. Blondel, P. Prettenhofer, R. Weiss, V. Dubourg, *et al.*, Scikit-learn: Machine learning in python, J. Mach. Learn Res. **12**, 2825 (2011).

[36] G. R. Stewart, Superconductivity in the A15 structure, Phys. C: Supercond. Appl. **514**, 28 (2015).

[37] E. Bustarret, Superconductivity in doped semiconductors, Phys. C: Supercond. Appl. **514**, 36 (2015).

[38] R. P. Smith, T. E. Weller, C. A. Howard, M. P. M. Dean, K. C. Rahnejat, S. S. Saxena, and M. Ellerby, Superconductivity in graphite intercalation compounds, Phys. C: Supercond. Appl. **514**, 50 (2015).

[39] R. A. Klemm, Pristine and intercalated transition metal dichalcogenide superconductors, Phys. C: Supercond. Appl. **514**, 86 (2015).

[40] O. Peña, Chevrel phases: Past, present and future, Phys. C: Supercond. Appl. **514**, 95 (2015).

[41] C. T. Wolowiec, B. D. White, and M. B. Maple, Conventional magnetic superconductors, Phys. C: Supercond. Appl. **514**, 113 (2015).

[42] S. L. Bud'ko and P. C. Canfield, Superconductivity of magnesium diboride, Phys. C: Supercond. Appl. **514**, 142 (2015).

[43] L. Ward, A. Agrawal, A. Choudhary, and C. Wolverton, A general-purpose machine learning framework for predicting properties of inorganic materials, npj Comput. Mater. **2**, 16028 (2016).

[44] B. Meredig, A. Agrawal, S. Kirklin, J. E. Saal, J. W. Doak, A. Thompson, K. Zhang, A. Choudhary, and C. Wolverton, Combinatorial screening for new materials in unconstrained composition space with machine learning, Phys. Rev. B **89**, 094104 (2014).

[45] W. Kohn and J. M. Luttinger, New mechanism for superconductivity, Phys. Rev. Lett. **15**, 524 (1965).

[46] V. Blum, R. Gehrke, F. Hanke, P. Havu, V. Havu, X. Ren, K. Reuter, and M. Scheffler, *Ab initio* molecular simulations with

numeric atom-centered orbitals, Comput. Phys. Commun. **180**, 2175 (2009).

[47] F. Knoop, T. A. R. Purcell, M. Scheffler, and C. Carbogno, FHI-vibes: Ab Initio vibrational simulations, J. Open Source Softw. **5**, 2671 (2020).

[48] M. H. Quenouille, Notes on bias in estimation, Biometrika **43**, 353 (1956).

[49] S. M. Lundberg and Su-In Lee, A unified approach to interpreting model predictions, in *Proceedings of the 31st International Conference on Neural Information Processing Systems (NIPS'17)* (Curran Associates Inc., Red Hook, NY, USA, 2017), pp. 4768–4777.

[50] M. T. Ribeiro, S. Singh, and C. Guestrin, Why should I trust you?: Explaining the predictions of any classifier, in *Proceedings of the 22nd ACM SIGKDD International Conference on Knowledge Discovery and Data Mining (KDD '16)* (ACM Press, New York, NY, USA, 2016), pp. 1135–1144.

[51] J. Herman and W. Usher, SALib: An open-source Python library for sensitivity analysis, J. Open Source Softw. **2**, 97 (2017).

[52] T. Iwanaga, W. Usher, and J. Herman, Toward SALib 2.0: Advancing the accessibility and interpretability of global sensitivity analyses, Socio-Environ. Syst. Modell. **4**, 18155 (2022).

[53] P. W. Anderson, Theory of dirty superconductors, J. Phys. Chem. Solids **11**, 26 (1959).

[54] D. Duan, Y. Liu, F. Tian, Huang Li, Zhao Z. X., H. Yu, B. Liu, W. Tian, and T. Cui, Pressure-induced metallization of dense $(H_2S)_2H_2$ with high-T_c superconductivity, Sci. Rep. **4**, 6968 (2014).

[55] D. Pelc, P. Popčević, M. Požek, M. Greven, and N. Barišić, Unusual behavior of cuprates explained by heterogeneous charge localization, Sci. Adv. **5**, eaau4538 (2019).

[56] P. D. Grigoriev, V. D. Kochev, A. P. Orlov, A. V. Frolov, and A. A. Sinchenko, Inhomogeneous superconductivity onset in FeSe studied by transport properties, Materials **16**, 1840 (2023).

[57] P. Mai, G. Balduzzi, S. Johnston, and T. A. Maier, Orbital structure of the effective pairing interaction in the high-temperature superconducting cuprates, npj Quantum Mater. **6**, 26 (2021).

[58] D. Rybicki, M. Jurkutat, S. Reichardt, C. Kapusta, and J. Haase, Perspective on the phase diagram of cuprate high-temperature superconductors, Nat. Commun. **7**, 11413 (2016).

[59] N. Kowalski, S. S. Dash, P. Sémon, D. Sénéchal, and A. Tremblay, Oxygen hole content, charge-transfer gap, covalency, and cuprate superconductivity, Proc. Natl. Acad. Sci. USA **118**, e2106476118 (2021).

[60] A. Kreisel, B. M. Andersen, P. O. Sprau, A. Kostin, J. C. Séamus Davis, and P. J. Hirschfeld, Orbital selective pairing and gap structures of iron-based superconductors, Phys. Rev. B **95**, 174504 (2017).

[61] K. Terashima, Y. Sekiba, J. H. Bowen, K. Nakayama, T. Kawahara, T. Sato, P. Richard, Y. Xu, L. J. Li, G. H. Cao, Z. Xu, H. Ding, and T. Takahashi, Fermi surface nesting induced strong pairing in iron-based superconductors, Proc. Natl. Acad. Sci. USA **106**, 7330 (2009).

[62] E. M. Nica, R. Yu, and Q. Si, Orbital-selective pairing and superconductivity in iron selenides, npj Quantum Mater. **2**, 24 (2017).

[63] S. Sykora and K. Becker, Heavy fermion properties of the Kondo Lattice model, Sci. Rep. **3**, 2691 (2013).

[64] A. O. Fumega and J. L. Lado, Nature of the unconventional heavy-fermion kondo state in monolayer CeSiI, Nano Lett. **24**, 4272 (2024).

[65] V. Stanev, C. Oses, A. G. Kusne, E. Rodriguez, J. Paglione, S. Curtarolo, and I. Takeuchi, Machine learning modeling of superconducting critical temperature, npj Comput. Mater. **4**, 29 (2018).

[66] B. T. Matthias, Empirical relation between superconductivity and the number of valence electrons per atom, Phys. Rev. **97**, 74 (1957).

[67] Z. Fan, J.-F. Zhang, B. Zhan, D. Lv, X.-Y. Jiang, B. Normand, and T. Xiang, Superconductivity in nickelate and cuprate superconductors with strong bilayer coupling, Phys. Rev. B **110**, 024514 (2024).

[68] S. M. O'Mahony, W. Ren, W. Chen, Y. X. Chong, X. Liu, H. Eisaki, S. Uchida, M. H. Hamidian, and J. C. S. Davis, On the electron pairing mechanism of copper-oxide high temperature superconductivity, Proc. Natl. Acad. Sci. USA **119**, e2207449119 (2022).

[69] X. Ma, G. Wang, R. Liu, T. Yu, Y. Peng, P. Zheng, and Z. Yin, Correlation-corrected band topology and topological surface states in iron-based superconductors,, Phys. Rev. B **106**, 115114 (2022).

[70] R. Yu, P. Goswami, Q. Si, P. Nikolic, and J.-X. Zhu, Superconductivity at the border of electron localization and itinerancy, Nat. Commun. **4**, 2783 (2013).

[71] K. Fan, H. Jin, B. Huang, G. Duan, R. Yu, Z. Y. Liu, H. N. Xia, L. S. Liu, Y. Zhang, T. Xie, Q. Y. Tang, *et al.*, Artificial superconducting Kondo lattice in a van der Waals heterostructure, Nat. Commun. **15**, 8797 (2024).

[72] D. R. Harshman and A. T. Fiory, Superconducting interaction charge in thallium-based High-T_c cuprates: Roles of cation oxidation state and electronegativity, J. Phys. Chem. Solids **85**, 106 (2015).

[73] C. Buzea and T. Yamashita, Correlation between electronegativity and superconductivity, Phys. B: Condens. Matter **281–282**, 951 (2000).

[74] G. W. Scheerer, Z. Ren, S. Watanabe, G. Lapertot, D. Aoki, D. Jaccard, and K. Miyake, The dominant role of critical valence fluctuations on high T_c superconductivity in heavy fermions, npj Quantum Mater. **3**, 41 (2018).

[75] C. Zhang, J. Huang, K. Zhai, K. Akhtari, Z. Shen, L. Ao, Z. Li, F. Qin, Y. Chang, L. Zhou, M. Tang, *et al.*, Valence-skipping and quasi-two-dimensionality of superconductivity in a van der Waals insulator, Nat. Commun. **13**, 6938 (2022).

[76] J. Bardeen, L. N. Cooper, and J. R. Schrieffer, Theory of Superconductivity, Phys. Rev. **108**, 1175 (1957).

[77] G. M. Eliashberg, Interactions between electrons and lattice vibrations in a superconductor, Sov. Phys. JETP **11**, 696 (1960).

[78] Y. Nambu, Quasi-particles and gauge invariance in the theory of superconductivity, Phys. Rev. **117**, 648 (1960).

[79] L. P. Gor'kov, On the energy spectrum of superconductors, Sov. Phys. JETP **34**, 505 (1958).

[80] A. B. Migdal, Interaction between electrons and lattice vibrations in a normal metal, Sov. Phys. JETP **34**, 996 (1958).

[81] W. L. McMillan, Transition temperature of strong-coupled superconductors, Phys. Rev. **167**, 331 (1968).

[82] P. B. Allen and R. C. Dynes, Transition temperature of strong-coupled superconductors reanalyzed, Phys. Rev. B **12**, 905 (1975).

[83] P. Morel and P. W. Anderson, Calculation of the superconducting state parameters with retarded electron-phonon interaction, Phys. Rev. **125**, 1263 (1962).

[84] G. A. Ummarino, Multiband superconductivity: Basic mechanisms and applications, Superconductivity **9**, 14 (2016).

[85] D. Mou, S. Manni, V. Taufour, Y. Wu, L. Huang, S. L. Bud'ko, P. C. Canfield, and A. Kaminski, Isotope effect on electron-phonon interaction in the multiband superconductor MgB_2, Phys. Rev. B **93**, 144504 (2016).

[86] J. Ahn and N. Nagaosa, Theory of optical responses in clean multi-band superconductors, Nat. Commun. **12**, 1617 (2021).

[87] N. W. Ashcroft and N. D. Mermin, *Solid State Physics* (Cengage Learning, Boston, MA, 1976), pp. 340–342.

[88] K. Kim, S. Kim, J. S. Kim, H. Kim, J.-H. Park, and B. I. Min, Importance of the van Hove singularity in superconducting $PdTe_2$, Phys. Rev. B **97**, 165102 (2018).

[89] Y. Luo, Y. Han, J. Liu, H. Chen, Z. Huang, L. Huai, H. Li, B. Wang, J. Shen, S. Ding, *et al.*, A unique van Hove singularity in kagome superconductor $CsV_{3-x}Ta_xSb_5$ with enhanced superconductivity, Nat. Commun. **14**, 3819 (2023).

[90] J. González, Microscopic description of d-wave superconductivity by Van Hove nesting in the Hubbard model, Phys. Rev. B **63**, 024502 (2000).

[91] C. Lane, R. Zhang, B. Barbiellini, R. S. Markiewicz, A. Bansil, J. Sun, and J.-X. Zhu, Competing incommensurate spin fluctuations and magnetic excitations in infinite-layer nickelate superconductors, Commun. Phys. **6**, 90 (2023).

[92] I. V. Leonov, Electronic structure and magnetic correlations in the trilayer nickelate superconductor $La_4Ni_3O_{10}$ under pressure, Phys. Rev. B **109**, 235123 (2024).

[93] D. R. Slocombe, V. L. Kuznetsov, W. Grochala, R. J. P. Williams, and P. P. Edwards, Superconductivity in transition metals, Philos. Trans. R. Soc. A **373**, 20140476 (2015).

[94] D. G. Pettifor, Theory of energy bands and related properties of 4d transition metals. I. Band parameters and their volume dependence, J. Phys. F: Met. Phys. **7**, 613 (1977).

[95] C. M. Varma and W. Weber, Phonon dispersion in transition metals, Phys. Rev. B **19**, 6142 (1979).

[96] G. D. Gaspari and B. L. Gyorffy, Electron-phonon interactions, *d* resonances, and superconductivity in transition metals, Phys. Rev. Lett. **28**, 801 (1972).

[97] W. E. Pickett, The next breakthrough in phonon-mediated superconductivity, Phys. C: Supercond. **468**, 126 (2008).